SCIEPublish

Article

Preparation of CdS-$BaZrO_3$ Heterojunction for Enhanced Photocatalytic Water-Splitting Hydrogen Production

Suhaib Shuaib Adam Shuaib *, Mengdie Cai *, Jun Zhang, Tengfei Ding, Pengcheng Wang, Yongshuai Chen and Song Sun

School of Chemistry and Chemical Engineering, Anhui University, Hefei 230601, China; 19856656450@139.com (J.Z.); DTF2022@163.com (T.D.); 1051495735@qq.com (P.W.); 522581519@qq.com (Y.C.); suns@ustc.edu.cn (S.S.)

* Corresponding author. E-mail: suhaibshuaib90@gmail.com (S.S.A.S.); caimengdie1987@163.com (M.C.)

Received: 23 July 2025; Accepted: 26 September 2025; Available online: 9 October 2025

ABSTRACT: Photocatalytic water splitting using solar light, a promising technical approach for hydrogen production. However, the slow charge transfer and rapid recombination of photogenerated charge carriers in photocatalysis limit their practical application. To address these issues, in this work, we successfully prepared a novel CdS-$BaZrO_3$ (CdS-BZO_3) heterojunction via a simple chemical-bath deposition method. The as-prepared heterojunctions facilitate the separation and transportation of photogenerated charges, while also maintaining the high redox-oxid ation ability of the photocatalysts. As a result, CdS-BZO_3 heterojunctions show enhanced photocatalytic water-splitting hydrogen production ability without a co-catalyst. Especially, the optimized CdS-BZO_3 sample exhibits high photocatalytic activity with a hydrogen production rate of 44.77 μmol/h, which is 4.4 and 2.9 times higher than that of BZO_3 and CdS, respectively. At the same time, the CdS-BZO_3 heterojunction exhibits good stability in the photocatalytic hydrogen production cycle test. This work provides a reference for the heterostructure construction of perovskite-based photocatalysts to improve photocatalytic performance.

Keywords: Photocatalysis; Perovskite; $BaZrO_3$/CdS; Type I heterojunction; Hydrogen production

1. Introduction

The pollution of the environment has worsened in recent decades due to the widespread usage of fossil fuels. It is consequently imperative to take advantage of clean, efficient, and sustainable options [1–3]. Producing hydrogen from water splitting using photocatalysis is a promising method of converting and using alternative energy [4,5]. Recently, perovskite materials have attracted considerable interest in the field of photocatalysis because of their remarkable stability, extensive crystal chemistry, and exceptional catalytic activity [5–9]. Among them, $BaZrO_3$ (BZO_3) possesses exceptional chemical and optical stability with a perovskite-oxide cubic structure, and its valence and conduction band edges are optimally matched with the redox potential of water, rendering it exceptionally well-suited for the process of photocatalytic hydrogen evolution [10–12]. However, the wide bandgap and rapid recombination of photogenerated charge carriers in BZO_3 limit its efficiency for photocatalytic water-splitting hydrogen evolution.

Some studies have shown that doping metal ions onto BZO_3 can inhibit the recombination of photogenerated charge carriers [13–17]. For example, Zhang et al. prepared Ce^{4+}-doped BZO_3 using the hydrothermal method [9]. Khan et al. synthesized a Ta-doped BZO_3 photocatalyst by the calcination method [10]. These photocatalysts improved the utilization of light, and they also demonstrated highly efficient photocatalytic water-splitting hydrogen evolution. However, it is important to note that doping can also introduce additional recombination centers, which can weaken the beneficial effects of doping. In addition, the process of optimizing doping content typically requires extensive experiments, which can be burdensome in terms of both time and energy consumption [18]. Recently, heterojunction construction has been widely implemented in the field of photocatalysis [19–22]. Combining BZO_3 with narrow band-gap semiconductors to construct heterojunctions will be an effective strategy for resolving the problem. As a result, the nanoscale interfacial contact facilitates the separation and movement of charges, decreases recombination, and ultimately results in improved photocatalytic water-splitting hydrogen production efficiency [23,24].

https://doi.org/10.70322/prp.2025.10018

In this context, cadmium sulfide (CdS) is a highly suitable alternative due to its good optical properties and narrow band-gap of approximately 2.4 eV [25]. It is an abundant, cost-effective, and easy-to-prepare material [26]. In addition, CdS can absorb light in the visible range, making it suitable for various photocatalytic applications [27]. In recent studies, CdS has been effectively employed in the construction of heterojunctions with semiconductors, including $Cs_{0.68}Ti_{1.83}O_4$ [28], TiO_2 [29], $SrTiO_3$ [30], and other materials for photocatalytic water-splitting hydrogen production processes [31,32]. However, after reviewing the existing literature, it has been determined that there are no previous reports on the coupling of BZO_3 with CdS for a photocatalytic water-splitting hydrogen evolution reaction under light radiation.

Herein, the CdS-BZO_3 heterostructure composites were successfully prepared via a simple chemical-bath deposition method, in which CdS is deposited on the surface of BZO_3, resulting in the formation of a heterojunction. The as-prepared heterojunctions not only facilitate the separation and transportation of photogenerated charges but also maintain the high redox-oxidation ability of the photocatalysts. Thus, CdS-BZO_3 heterojunctions exhibit improved photocatalytic water-splitting hydrogen production performance, even without the addition of a noble-metal co-catalyst. Out of all the CdS content, the CdS-BZO_3-3 demonstrated the best results for photocatalytic hydrogen production, with a hydrogen production rate of 44.77 μmol/h under simulated sunlight irradiation, which is 4.4 and 2.9 times higher than that of BZO_3 and CdS, respectively. This paper provides a useful reference for further research on the construction of heterostructures for enhanced photocatalytic performance.

2. Materials and Methods

2.1. Chemicals and Materials

Barium chloride dihydrate ($BaCl_2 \cdot 2H_2O$) and Zirconium oxychloride ($ZrOCl_2 \cdot 8H_2O$) were provided by Aladdin Reagent Co., Ltd. (Shanghai, China). Cadmium chloride ($CdCl_2$), Ammonium chloride (NH_4Cl), Sodium sulfide nonahydrate ($Na_2S \cdot 9H_2O$), and Sodium sulfite ($Na_2SO_3 \cdot xH_2O$) were provided by Shanghai Sinopharm Chemical Reagent Co., Ltd. (Shanghai, China). Chloroplatinic acid (H_2PtC_{l6}), Thiourea (CN_2H_4S), and Ammonium hydroxide ($NH_3 \cdot H_2O$) were provided by Shanghai Macklin Biochemical Co., Ltd. (Shanghai, China). Sodium hydroxide (NaOH) and ethanol were provided by Tianjin Damao Chemical Reagent Co., Ltd. (Tianjin, China). Deionized water was provided by local sources. All the chemicals were used in their original state without undergoing any additional purification processes.

2.2. Preparation of BZO_3

The calculated amounts of $BaCl_2 \cdot 2H_2O$ and $ZrOCl_2 \cdot 8H_2O$ were first dissolved in 20 mL of deionized water with magnetic stirring and heated until the solution became transparent. Subsequently, a solution of 15 M NaOH was gradually added to the transparent solution while vigorously stirring, leading to the formation of precipitated hydroxides. The resulting mixture was then enclosed in a Teflon-lined stainless-steel autoclave and subjected to a temperature of 180 °C for 12 h. Finally, the BZO_3 product was obtained after the resulting substances were washed with deionized water and ethanol multiple times and dried at 80 °C overnight.

2.3. Preparation of CdS-BZO_3 Heterojunction

Initially, 0.2 g of BZO_3 was dispersed in water using ultrasonic waves. Subsequently, 0.34 g of $CdCl_2$, 0.16 g of NH_4Cl, and 0.57 g of $CS(NH_2)_2$ were added to the mixture and vigorously stirred at room temperature for 2 h. Following this, $NH_3 \cdot H_2O$ was gradually dropped to adjust the pH to 9 in the solution. After allowing for a certain period of additional reaction time, the resulting suspension was centrifuged, washed multiple times with water and ethanol, and dried at 60 °C under vacuum for 12 h. The final products with different weight ratios of CdS to BZO_3 (25%, 35%, 50%, and 75%) were named CdS-BZO_3-1, CdS-BZO_3-2, CdS-BZO_3-3, and CdS-BZO_3-4, respectively. As a comparison, pure CdS was also prepared using the same reaction conditions, except that no BZO_3 was added.

2.4. Characterization of Samples

The crystal phase of the BZO_3, CdS, and CdS-BZO_3 was characterized using X-ray diffraction (XRD, Rigaku Corporation, Japan) with Cu Kα radiation (λ = 1.5418 Å), utilizing a Smartlab 9 kW instrument. The morphologies of the samples were determined by scanning electron microscopy (SEM, Regulus 8230, Hitachi, Japan) and transmission electron microscopy (TEM, JEM-2010, JEOL, Tokyo, Japan). X-ray photoelectron spectroscopy (XPS, Escalab 250Xi, Waltham, MA, USA) was employed to examine and analyze the chemical composition of the samples. The

photoluminescence (PL) spectra and time-resolved photoluminescence spectra (TRPL) were recorded with FLUORMAX-4P (HORIBA JOBIN YUON, Palaiseau, France). The UV-vis diffuse reflectance spectra (DRS) were conducted by conducting measurements on a UV-visible spectrometer (Hitachi U-4100, Tokyo, Japan) within the wavelength range of 200–800 nm. To ensure accuracy, $BaSO_4$ was used as the background during the measurements. The electrochemistry workstation (CHI 660, CH Instrument, Bee Cave, TX, USA) was utilized to conduct photoelectrochemical measurements using a three-electrode system. In this system, the Pt electrode served as the counter electrode, while the Ag/AgCl electrode functioned as the reference electrode. The working electrode was prepared using 10 mg of the sample, 0.02 mL of Nafion, and 0.4 mL of ethanol to make a slurry. This slurry was then deposited onto glass substrates coated with FTO thin films. The tests were carried out at room temperature, using a 0.5 M Na_2SO_4 aqueous solution as an electrolyte.

2.5. Hydrogen Production Experiments

The photocatalytic activities were performed by a photocatalytic reaction system (MC-SPB10, Beijing Merry Change Technology Co., Ltd., Beijing, China). The glass-reaction vessel was employed in the system to carry out the photocatalytic water-splitting reactions. In a standard experiment, 50 mg of each sample was dispersed in a 50-mL aqueous solution containing 0.1 M Na_2S and 0.05 M Na_2SO_3. The Na_2S/Na_2SO_3 combination served as a sacrificial agent. To ensure the removal of air, the system was evacuated for 10 min and purged with argon three times. The light source for the reactions was a 300 W Xe lamp (MC-PF300C, Beijing Merry Change Technology Co., Ltd., emitting in the 200–1100 nm wavelength range). The pictures and spectrum of the xenon lamp used in the experiment have been provided in the supporting information (Figures S1 and S2, respectively). The hydrogen products were measured using online gas chromatography (GC-5190, Anhui Chromatography Co., Ltd., Hefei, China) with argon as the carrier gas.

3. Results and Discussion

The crystallinity and structure of BZO_3, CdS, and CdS-BZO_3 samples were analyzed using X-ray diffraction (XRD) analysis. As shown in Figure 1, BZO_3 exhibits a highly crystalline pattern, with narrow and well-defined peaks between diffraction angles 10° and 80°. The XRD pattern obtained aligns perfectly with JCPDS standard No. 74-1299, which corresponds to the tetragonal perovskite-type cubic structure of $BaZrO_3$. On the other hand, CdS displayed weak diffraction peaks, which are well-indexed to hexagonal CdS (JCPDS No. 77-2306). For CdS-BZO_3-3 heterojunction, as can be seen, except for the peaks of BZO_3 and CdS, no extra peak was identified, which confirms the successful synthesis of CdS-BZO_3 heterostructures.

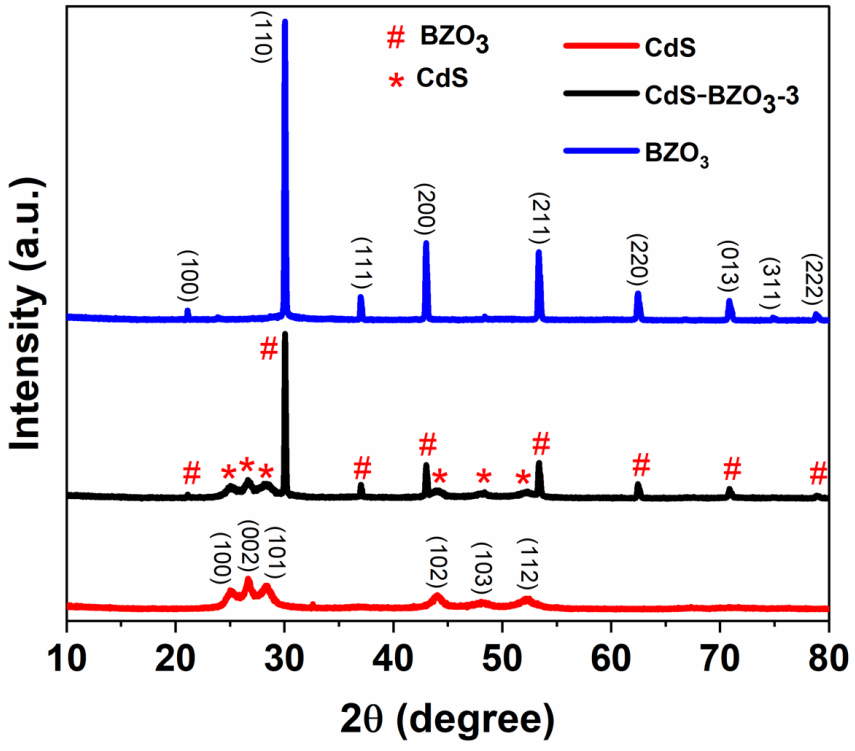

Figure 1. XRD patterns of CdS, CdS-BZO_3-3 heterojunction, and BZO_3.

SEM was conducted to examine the morphologies of BZO_3, CdS, and CdS-BZO_3. As shown in Figure 2a,d, BZO_3 possesses a cubic structure, which can facilitate the electron-hole pairs generated during the process [33,34]. On the other hand, CdS shows the morphology of nanosheets, consistent with previous findings (Figure 2b,e) [35]. Figure 2c,f display the SEM images of the CdS-BZO_3 heterojunction. The attachment of CdS nanosheets onto the surface of BZO_3 is evident. The structure of the CdS-BZO_3 composite remains consistent with that of pure BZO and CdS, indicating that the composite primarily consists of BZO_3 and CdS. These findings are consistent with the XRD characterization results.

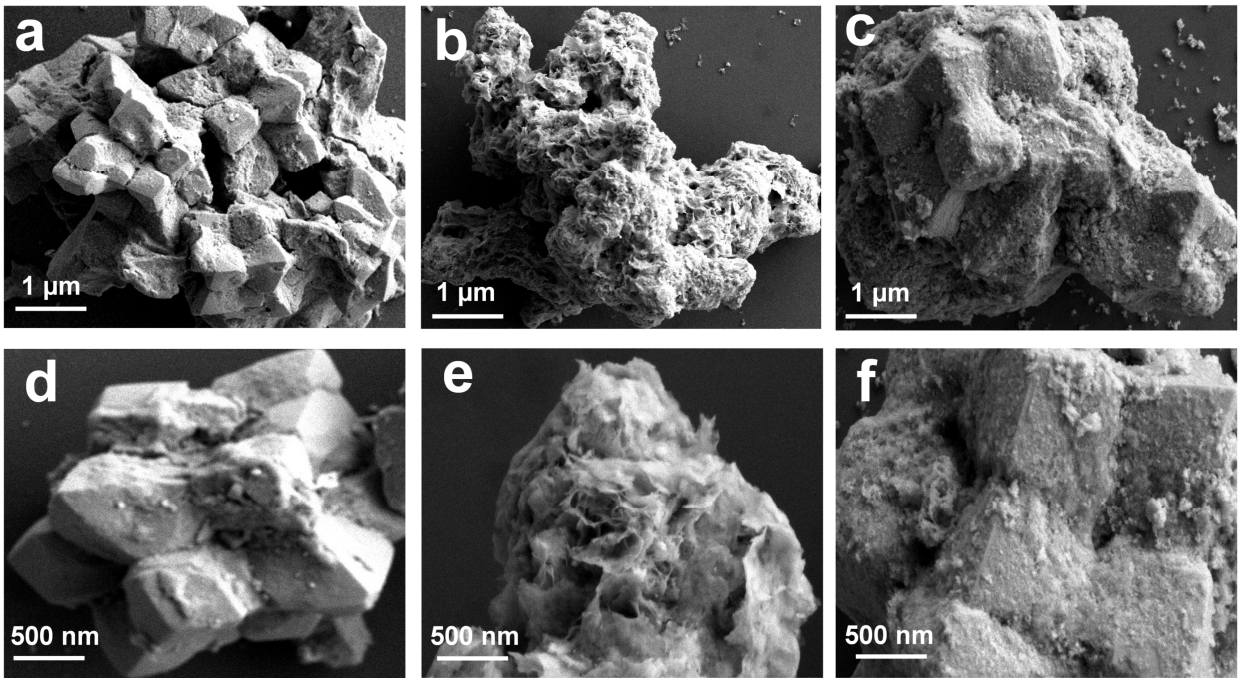

Figure 2. SEM images of (**a**,**d**) BZO3, (**b**,**e**) CdS, and (**c**,**f**) CdS-BZO_3 heterojunction.

The morphology and microstructure of the CdS-BZO_3 heterojunction were further examined by transmission electron microscopy (TEM). The cubic structure of CdS-BZO_3 can be observed in Figure 3a, which matches the SEM observation. The high-resolution TEM (HRTEM) image of CdS-BZO_3 (Figure 3b) displays interplanar spacing of 0.29 nm and 0.33 nm, aligning to the (110) lattice plane for BZO_3 and the (002) lattice plane for CdS, respectively. The close contact between the phases of BZO_3 and CdS in the CdS-BZO_3 sample demonstrates the formation of a heterojunction between the two materials, which is advantageous for the separation of photogenerated electron-hole pairs to support the enhancement of photocatalytic performance. Furthermore, the energy-dispersive X-ray spectrometry (EDX) elemental maps show the distribution of Ba, Zr, O, Cd, and S elements in CdS-BZO_3 composites (Figure 3c–h), which demonstrates that the BZO_3 nano-cubes are successfully combined with CdS. In addition, the Pt co-catalyst photo-deposition sites can provide evidence of the successful preparation of the heterojunction. The high-resolution TEM image in Figure S3 shows that Pt nanoparticles are deposited on the surface of CdS, not on the surface of BZO_3. This further validates the successful preparation of the CdS-BZO_3 heterojunction, proves that CdS is the main photo-deposition site in the heterojunction, and also confirms the movement of photogenerated electrons from BZO_3 to CdS in the heterojunction.

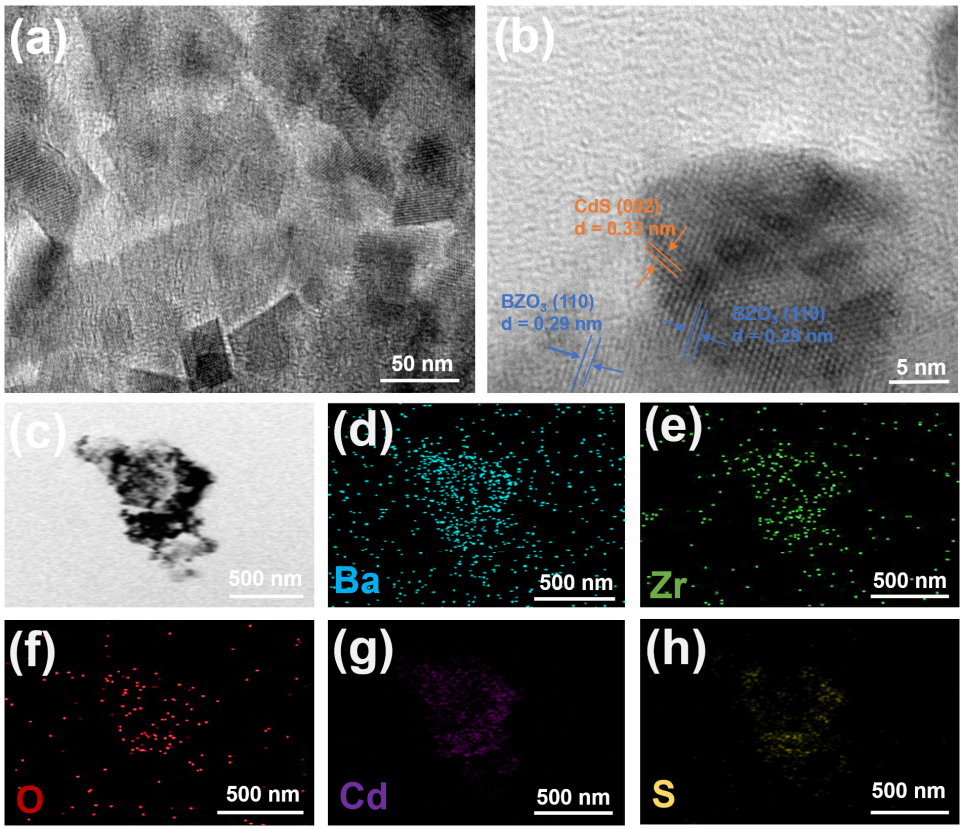

Figure 3. (**a**) TEM; (**b**) High-resolution TEM; (**c**–**h**) EDS-mapping of CdS-BZO_3-3 sample.

The surface chemical compositions of BZO_3, CdS, and CdS-BZO_3 were validated using an X-ray photoelectron spectrometer (XPS). Figure 4 displays the high-resolution XPS spectra of Ba 3d, Zr 3d, O 1s, Cd 3d, and S 2p for the samples. As depicted in Figure 4a, the Ba 3d photoelectron peaks of CdS-BZO_3 are located at around 780.1 eV and 795.5 eV for the Ba $3d_{3/2}$ and Ba $3d_{5/2}$ lines, respectively. Compared to the Ba 3d peaks of pure BZO_3 (779.6 and 794.9 eV), these peaks are shifted to a higher binding-energy side, indicating a strong electronic coupling interaction between BZO_3 nano-cubes and CdS nanosheets [28]. Furthermore, the Zr 3d peaks of CdS-BZO_3 also show a shift towards higher binding energy compared to the pure BZO_3 peaks at 184.2 and 181.9 eV (Figure 4b). This shift of 0.4~0.5 eV is primarily due to the strong electronic coupling between BZO_3 and CdS. It is believed that electrons in BZO_3 transfer to CdS, which is beneficial for photocatalysis. The Cd 3p XPS spectrum of pure CdS (Figure 4c) displays peaks at 411.9 and 405.1 eV, which can correspond to Cd $3d_{3/2}$ and Cd $3d_{5/2}$, respectively. These peaks are characteristic of Cd^{2+} in CdS [36,37]. In Figure 4d, the S 2p spectrum of pure CdS shows peaks at 162.5 and 161.4 eV, corresponding to S $2p_{1/2}$ and S $2p_{3/2}$, respectively [36,37]. For the CdS-BZO_3 heterojunction as shown in Figure 4c,d, both the Cd 3p and S 2p spectra shift to higher binding energies compared to those for pure CdS, which reinforces the evidence of electron transfer from BZO_3 to CdS. The increase in electron density on CdS implies that more photogenerated electrons could be engaged in the hydrogen production reaction over the CdS-BZO_3 heterojunction under light irradiation.

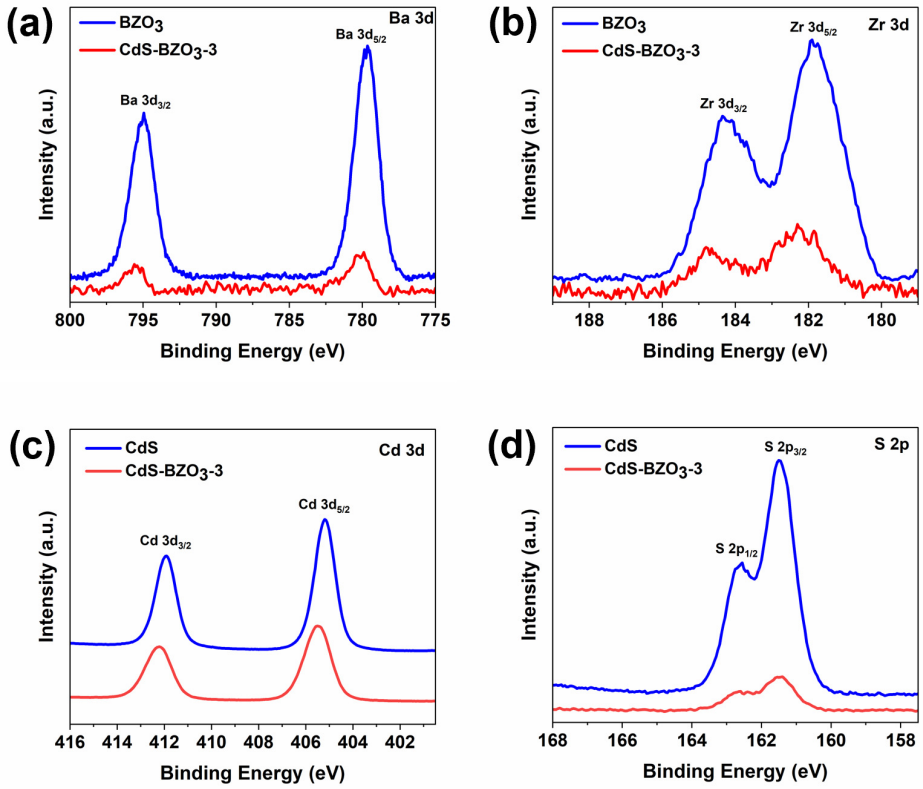

Figure 4. High-resolution XPS spectrum for (**a**) Ba 3d; (**b**) Zr 3d; (**c**) Cd 3d; (**d**) S 2p of BZO_3, CdS, and CdS-BZO_3-3 heterojunction.

The optical properties of the prepared samples were investigated using UV-vis diffuse-reflectance spectra (DRS). As shown in Figure 5a, the results indicate that CdS exhibits strong absorption in the visible region, with absorption edges at around 540 nm. Notably, CdS-BZO_3 exhibited a distinct shift where the absorption edges extended into the visible light region, unlike pure BZO_3. Due to the CdS being a direct semiconductor and BZO_3 being an indirect semiconductor, their band-gap could be estimated by determining the point of the tangents on the plots of $(\alpha h\nu)^2$ versus photon-energy ($h\nu$) and $(\alpha h\nu)^{1/2}$ versus photon-energy ($h\nu$), respectively [38,39]. Figure 5b displays that the estimated band-gap for CdS is approximately 2.4 eV, while BZO_3 has a band-gap of around 4.89 eV, which aligns with findings from previous research [29,38].

Mott-Schottky tests were performed to determine the conduction band (CB) potentials of CdS and BZO_3. As depicted in Figure 5c,d, both BZO_3 and CdS exhibited characteristics of n-type semiconductors, and their flat-band potentials (E_{fb}) are determined to be −1.49 V and −0.67 V versus Ag/AgCl, respectively. This was accomplished by extending the linear part of the Mott-Schottky plots to cross the longitudinal axis at zero [40]. The E_{fb} versus EAg/AgCl can be described with the normal hydrogen electrode (NHE) using the Nernst equation: $E_{NHE} = E_{Ag/AgCl} + 0.197$ V, where BZO_3 and CdS are respectively determined to be −1.29 and −0.47 V (*vs.* NHE). The E_{fb} of n-type semiconductors is closely associated with the conduction band (CB) and is approximately 0.1 V more positive than its conduction band potentials (E_{CB}) [41]. So, the E_{CB} of BZO_3 and CdS is approximately calculated to be around −1.39 and −0.57 V (*vs.* NHE). Additionally, according to the equation of $E_g = E_{VB} - E_{CB}$, the valence bands (VB) of BZO_3 and CdS were calculated to be 3.5 and 1.83 eV, respectively [42]. Consequently, as predicted, the formation of a Type I heterojunction between BZO_3 and CdS, a typical structure for electron and hole separation with staggered alignment, is possible.

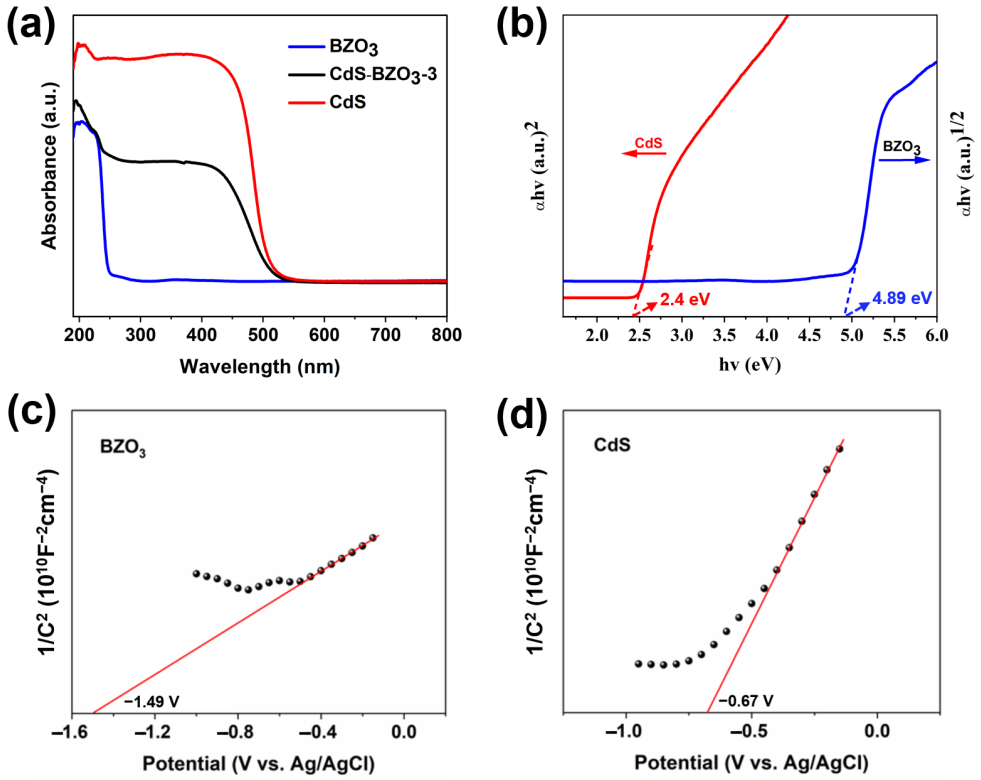

Figure 5. (**a**) UV–vis absorption spectra of BZO_3, CdS-BZO_3-3 heterojunction, and CdS; (**b**) The calculated band-gap of BZO_3 and CdS, Mott-Schottky plots of (**c**) BZO_3 and (**d**) CdS.

The photoluminescence (PL) spectra of the samples were acquired to study the separation and transfer processes of the photogenerated charges in the materials. Figure 6a demonstrates that emission peaks in all the samples displayed are centered at approximately 503 nm. Pure CdS demonstrates a strong peak intensity in its photoluminescence, indicating that the recombination of photogenerated electron-hole pairs occurs easily. However, when CdS is combined with BZO_3, the photoluminescence peak intensity gradually diminishes. Notably, CdS/BZO_3-3 exhibits the lowest photoluminescence peak intensity, suggesting that its efficiency in separating electron-hole pairs is significantly enhanced, effectively suppressing the recombination of photogenerated electron-hole pairs. The time-resolved PL spectra of prepared samples are depicted in Figure 6b. In contrast to CdS and BZO_3, the CdS-BZO_3-3 heterojunction exhibits a slow decay characteristic. The calculated average lifetime of CdS-BZO_3-3 is 404 ps, which is 3 times longer than that of CdS and 7 times longer than that of BZO_3. These findings suggest that the CdS-BZO_3 heterojunctions promote electron transfer, effectively suppressing the recombination of photogenerated electron-hole pairs.

To further investigate the separation and migration of electron-hole pairs, photocurrent measurement of CdS, BZO_3, and CdS/BZO_3 was performed. As depicted in Figure 6c, when subjected to periodic circular light illumination with 20-s intervals, all the working electrodes exhibit a rapid rise in photocurrent density, reaching a stable state. However, upon turning off the light, the photocurrent experiences a substantial decrease. Interestingly, it is noted that the steady photocurrent density of the CdS-BZO_3-3 heterojunction is considerably higher compared to that of pure CdS and BZO_3. This observation suggests that the CdS-BZO_3 heterojunction effectively mitigates the recombination of photoexcited charges, leading to enhanced charge separation and a sustained photocurrent response. Electrochemical impedance spectroscopy (EIS) was used to study the charge transfer process taking place at the interface between the photoelectrodes and the electrolyte. This was done by measuring Nyquist plots under illumination. Figure 6d presents Nyquist plots for pristine CdS, BZO_3, and the CdS-BZO_3-3 samples. CdS-BZO_3-3 shows a smaller semicircle plot compared to those of pristine CdS and BZO_3. This observation indicates a reduced resistance to charge migration across the interface between BZO_3 and CdS. Overall, the results of photoluminescence, photocurrent, and impedance measurements can be used to demonstrate the high photocatalytic performance of the CdS-BZO_3 heterojunctions.

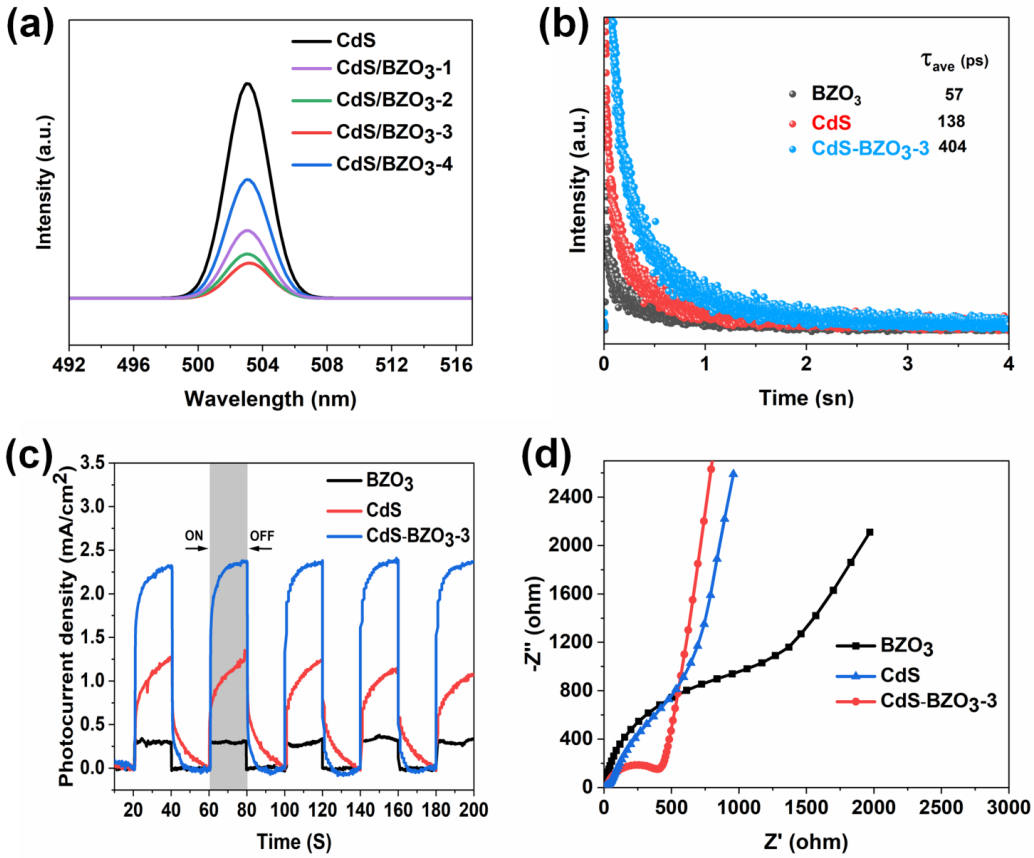

Figure 6. (**a**) Photoluminescence (PL) spectra of CdS and CdS-BZO_3 heterojunctions; (**b**) Time-resolved photoluminescence spectra, (**c**) Transient photocurrent response spectra, and (**d**) electrochemical impedance spectroscopy spectra of BZO_3, CdS, and CdS-BZO_3-3 heterojunction.

The hydrogen production performance of BZO_3, CdS, and CdS-BZO_3 heterojunctions was determined by conducting a photocatalytic water-splitting test under full-spectrum illumination. As depicted in Figure 7a, pure BZO_3 and CdS show low photocatalytic hydrogen production performance, which could be because of the rapid recombination of electron-hole pairs. In contrast, the photocatalytic hydrogen production activity is significantly improved when coupling BZO_3 with CdS, reaching a maximum value of 44.77 μmol/h on the CdS-BZO_3-3 sample. In addition, as shown in Figure 7b, the photocatalytic rate of hydrogen production on CdS-BZO_3 samples gradually rises with increasing CdS content. Nevertheless, as the CdS content continues to increase, the rate of hydrogen production decreases, potentially attributable to the limited light-harvesting capacity of BZO_3 nano-cubes. To further investigate the visible-light-driven photocatalytic performance, the hydrogen production rates of BZO_3, CdS, and CdS-BZO_3 heterojunctions were evaluated under visible-light irradiation, as illustrated in Figure 7c. Pure BZO_3 exhibits no detectable hydrogen production activity due to its wide band gap, which restricts absorption in the visible-light region. In contrast, pure CdS shows a relatively high hydrogen production rate of 9.12 μmol/h under visible light. The CdS-BZO_3-3 heterojunction achieves a hydrogen production rate of 6.37 μmol/h, which is lower than that of pure CdS. This result suggests that under visible-light irradiation, the photocatalytic activity is mainly governed by CdS, while the incorporation of BZO_3 does not directly contribute to visible-light harvesting. Instead, the partial decrease in activity can be attributed to the reduced effective light absorption of CdS when coupled with BZO_3. Therefore, the advantage of introducing BZO_3 into CdS becomes more evident under full-spectrum illumination, where both components can synergistically participate in the photocatalytic process. To examine the reusable capabilities and long-term stability of the CdS-BZO_3 heterojunctions, four cycles of photocatalytic hydrogen production were conducted on the CdS-BZO_3-3 sample, and the findings are displayed in Figure 7d. The photocatalytic hydrogen production performance of CdS-BZO_3-3 did not significantly change after four test cycles, indicating its outstanding stability during long-term photocatalytic processes. In addition, to further evaluate the structural and chemical stability of the catalyst after the photocatalytic reaction, XPS, XRD, and UV–vis absorption analyses were performed on the used CdS-BZO_3-3 sample (Figure S4). The high-resolution XPS spectra (Figure S4a–d) reveal that the binding energies of Ba 3d, Zr 3d, Cd 3d, and S 2p remain essentially unchanged compared with the fresh sample, indicating the preservation of the chemical states of the constituent elements. The XRD pattern (Figure S4e) confirms that the crystalline phases of CdS and BZO_3

are well retained after photocatalysis, with no new impurity peaks detected, suggesting that the heterojunction structure remains intact. Moreover, the UV–vis absorption spectrum (Figure S4f) shows no obvious shift in the absorption edge, demonstrating that the optical properties of CdS-BZO_3-3 are maintained after the reaction. Taken together, the results from the cycling test and post-characterization confirm that the CdS-BZO_3 heterojunction not only exhibits high photocatalytic hydrogen evolution activity but also possesses excellent structural, chemical, and optical stability, making it a promising photocatalyst for long-term water-splitting applications.

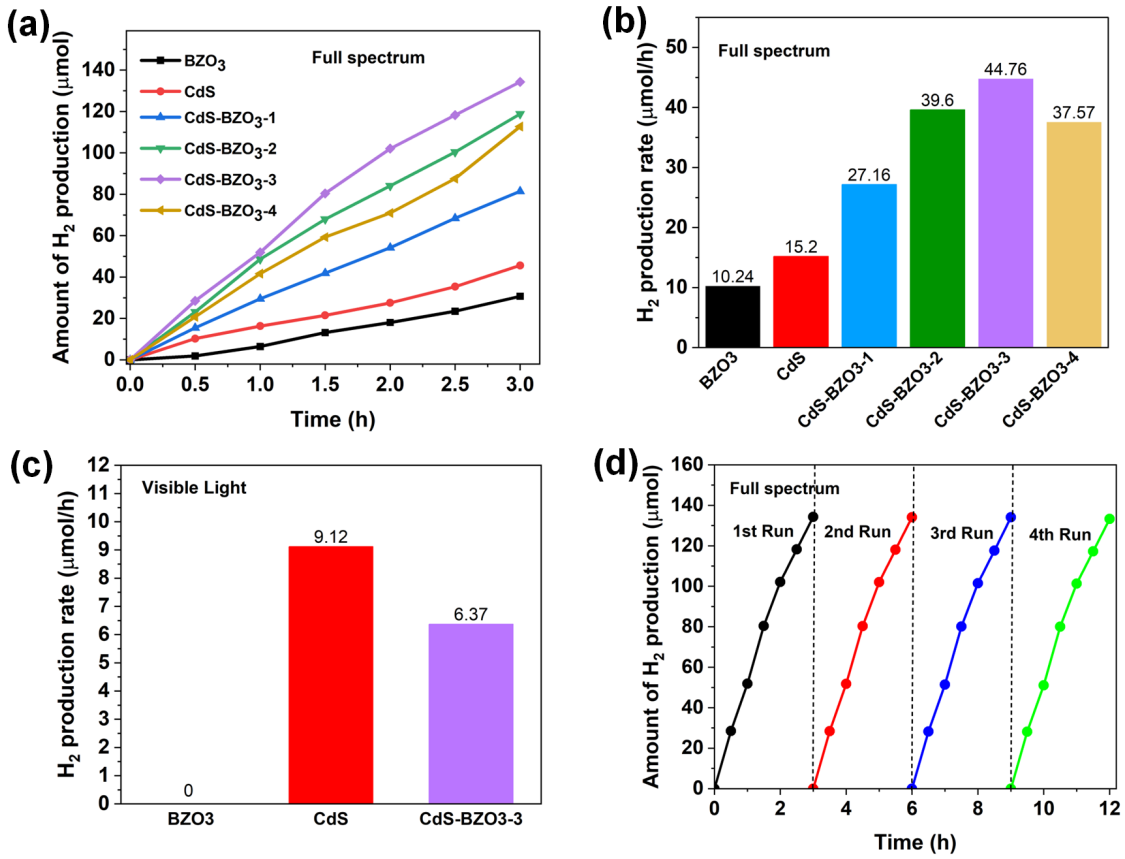

Figure 7. (**a**) Time courses of photocatalytic water-splitting hydrogen production and (**b**) Average hydrogen production rates of BZO_3, CdS, and CdS-BZO_3 heterojunctions under full spectrum. (**c**) Average hydrogen production rates of BZO_3, CdS, and CdS-BZO_3 heterojunctions under visible light. (**d**) Stability experiment of CdS-BZO_3-3 for photocatalytic water-splitting hydrogen production under full spectrum.

Based on the comprehensive measurements mentioned above, the potential mechanism for photocatalytic water-splitting hydrogen production of the CdS-BZO_3 heterojunction is depicted in Figure 8. The initial energy band structure before contact was determined experimentally by ultraviolet photoelectron spectroscopy (UPS), as shown in Figure 8a. The secondary electron cutoff (SEC) and valence band (VB) spectra were used to calculate the work functions (Φ) and ionization potentials. The work function (Φ) of a material, given by $\Phi = h\nu - E_{cut\ off}$ (where $h\nu = 21.22$ eV for the He I source), was found to be 4.88 eV for BZO_3 and 5.16 eV for CdS. This key difference indicates that BZO_3 has a higher Fermi level (E_F) than CdS. Consequently, as Figure 8c illustrates, when the CdS-BZO_3 heterostructure forms, electrons spontaneously migrate from BZO_3 to CdS until their Fermi levels equilibrate. This electron transfer creates a positively charged interface region on the BZO_3 side, causing its band edge to bend upward and form an electron depletion layer. Conversely, the band edge of CdS bends downward due to the accumulation of electrons. This process results in the formation of a strong built-in electric field directed from BZO_3 to CdS at the interface. Subsequently, as shown in Figure 8d, when the CdS-BZO_3 heterojunction is exposed to light irradiation, both BZO_3 and CdS absorb photons and generate electron-hole pairs. Driven by the synergistic effects of the band edge bending, the built-in electric field, and Coulomb interaction, photogenerated electrons in the CB of BZO_3 readily transfer to recombine with the holes in the VB of CdS. This Z-scheme charge transfer mechanism effectively accumulates electrons in the CB of CdS, which possesses a sufficiently negative potential to reduce H^+ to H_2. Simultaneously, the photogenerated holes from the valence band of BZO_3 transfer to the valence band of CdS, where they are consumed by the sacrificial agents (Na_2S/Na_2SO_3), thus preventing photocorrosion and completing the redox cycle. Consequently, the

CdS-BZO_3 heterojunction, with its band alignment quantitatively established by UPS, exhibits a highly efficient Z-scheme charge transfer pathway. This mechanism significantly improves the separation and transport of photogenerated electron-hole pairs, leading to the dramatically enhanced photocatalytic water-splitting hydrogen production performance.

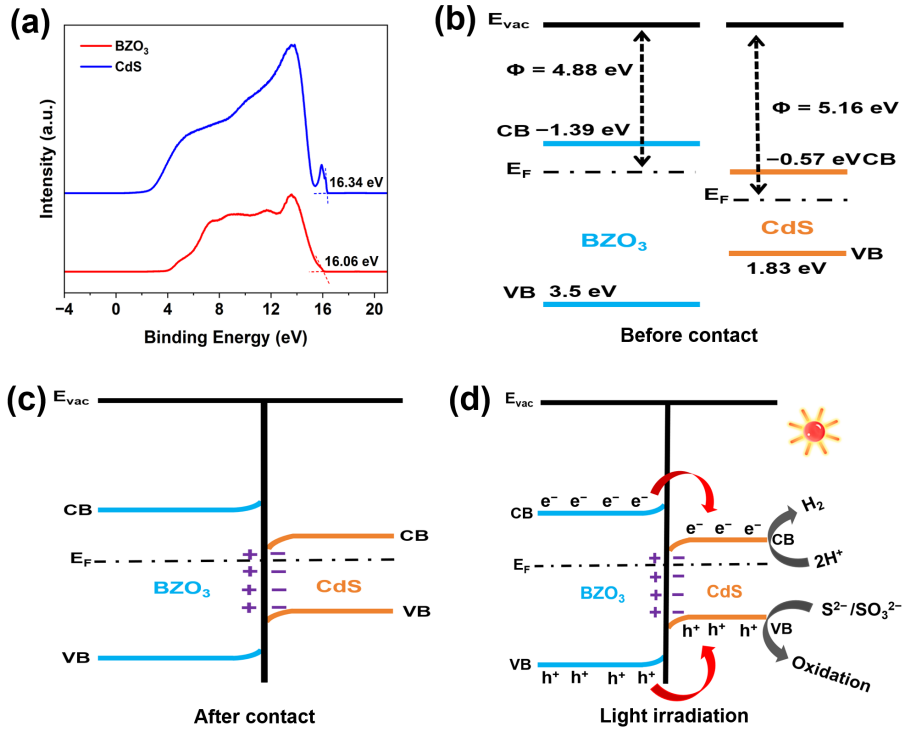

Figure 8. (**a**) The UPS spectra of CdS and BZO_3, schematic diagrams of the proposed photocatalytic mechanism of CdS-BZO_3 heterojunction for photocatalytic water splitting hydrogen production (**b**) before contact, (**c**) after contact, and (**d**) under light irradiation.

4. Conclusions

In summary, BZO_3 was initially prepared via the hydrothermal method, followed by the deposition of CdS on its surface through a simple chemical-bath deposition method to obtain a heterostructure composite. The resulting CdS-BZO_3 heterojunction demonstrates high performance in hydrogen production rate (44.77 μmol/h) without the addition of a noble-metal co-catalyst, a significant enhancement compared to pure BZO_3 (10.25 μmol/h) and CdS (15.2 μmol/h). The notable enhancement in the performance of the CdS-BZO_3 heterojunction could be due to its effective separation and transfer of photogenerated charge, the reduction of electron-hole pair recombination, and the maintenance of high reduction-oxidation ability. The experimental findings suggest a potential water-splitting photocatalytic hydrogen production mechanism of the CdS-BZO_3 heterojunction under simulated sunlight illumination. This work provides a strong reference for heterostructure construction and further improvements in perovskite-based photocatalysts.

Supplementary Material

The following supporting information can be found at: https://www.sciepublish.com/article/pii/707, Figure S1: The xenon lamp light source system. Figure S2: The spectrum of the xenon lamp light source system. Figure S3: High-resolution TEM image of CdS-BZO_3-3 sample after photochemical deposition of Pt. Figure S4. High-resolution XPS spectrum for (a) Ba 3d; (b) Zr 3d; (c) Cd 3d; (d) S 2p, (e) XRD patterns, and (f) UV–vis absorption spectra of used CdS-BZO_3-3 heterojunction.

Author Contributions

Conceptualization, S.S.A.S. and S.S.; Methodology, S.S.A.S., M.C. and J.Z.; Software, S.S.A.S.; Validation, M.C., P.W. and Y.C.; Formal Analysis, S.S.A.S. and T.D.; Investigation, M.C.; Resources, S.S.A.S. and M.C.; Data Curation, S.S.A.S.; Writing—Original Draft Preparation, S.S.A.S.; Writing—Review & Editing, S.S.A.S. and M.C.; Visualization, M.C.; Supervision, S.S.; Project Administration, S.S.; Funding Acquisition, S.S.

Ethics Statement

Not applicable.

Informed Consent Statement

Not applicable.

Data Availability Statement

The data that support the findings of this study are available from the corresponding author upon reasonable request.

Funding

This work is supported by the National Natural Science Foundation of China (22308001, 21902001, and 22179001), Higher Education Natural Science Foundation of Anhui Province (KJ2021A0029 and KJ2021A0027), Distinguished Young Research Project of Anhui Higher Education Institution (022AH020007), The University Synergy Innovation Program of Anhui Province (GXXT-2023-009).

Declaration of Competing Interest

The authors declare that they have no known competing financial interests or personal relationships that could have appeared to influence the work reported in this paper.

References

1. Shuaib SSA, Niu Z, Qian Z, Qi S, Yuan W. Self-luminous, shape-stabilized porous ethyl cellulose phase-change materials for thermal and light energy storage. *Cellulose* **2023**, *30*, 1841–1855. doi:10.1007/s10570-022-05030-4.
2. Fu J, Yu J, Jiang C, Cheng B. g-C_3N_4-based heterostructured photocatalysts. *Adv. Energy Mater.* **2018**, *8*, 1701503. doi:10.1002/aenm.201701503.
3. Shuaib SSA, Yuan W. Hierarchical magnetic porous carbonized wood composite phase change materials for efficient solar-thermal, electrothermal, and magnetothermal conversion-storage. *Mater. Today Commun.* **2023**, *37*, 107486. doi:10.1016/j.mtcomm.2023.107486.
4. Cai M, Wang X, Xue J, Jiang Y, Wei Y, Cheng Q, et al. Improvement of photocatalytic hydrogen evolution of $La_5Ti_2AgS_5O_7$ by flash sintering method. *Appl. Phys. Lett.* **2021**, *119*, 073901. doi:10.1063/5.0059553.
5. Lu L, Ni S, Liu G, Xu X. Structural dependence of photocatalytic hydrogen production over La/Cr co-doped perovskite compound $ATiO_3$ (A = Ca, Sr and Ba). *Int. J. Hydrogen Energy* **2017**, *42*, 23539–23547. doi:10.1016/j.ijhydene.2017.07.216.
6. Sobahi TR, Amin MS. Photocatalytic oxidation of atrazine using $BaTiO_3$-MWCNT nanocomposites under visible light. *Ceram. Int.* **2021**, *47*, 14366–14374. doi:10.1016/j.ceramint.2021.01.187.
7. Iervolino G, Vaiano V, Sannino D, Rizzo L, Ciambelli P. Production of hydrogen from glucose by $LaFeO_3$ based photocatalytic process during water treatment. *Int. J. Hydrogen Energy* **2016**, *41*, 959–966. doi:10.1016/j.ijhydene.2015.11.030.
8. Jana P, de la Peña O'Shea VA, Mata Montero C, Pizarro P, Coronado JM, Fresno F, et al. Factors influencing the photocatalytic activity of alkali Nb Ta perovskites for hydrogen production from aqueous methanol solutions. *Int. J. Hydrogen Energy* **2016**, *41*, 19921–19928. doi:10.1016/j.ijhydene.2016.08.135.
9. Zhang H, Qiao J, Li G, Li S, Wang G, Wang J, et al. Preparation of Ce^{4+}-doped $BaZrO_3$ by hydrothermal method and application in dual-frequent sonocatalytic degradation of norfloxacin in aqueous solution. *Ultrason. Sonochem.* **2018**, *42*, 356–367. doi:10.1016/j.ultsonch.2017.12.035.
10. Khan Z, Qureshi M. Tantalum doped $BaZrO_3$ for efficient photocatalytic hydrogen generation by water splitting. *Catal. Commun.* **2012**, *28*, 82–85. doi:10.1016/j.catcom.2012.08.005.
11. Chen T, Meng J, Lin Q, Wei X, Li J, Zhang Z. One-step synthesis of hollow $BaZrO_3$ nanocrystals with oxygen vacancies for photocatalytic hydrogen evolution from pure water. *J. Alloys Compd.* **2019**, *780*, 498–503. doi:10.1016/j.jallcom.2018.11.306.
12. Huerta-Flores AM, Mora-Hernández JM, Torres-Martínez LM, Moctezuma E, Sánchez-Martínez D, Zarazúa-Morín ME, et al. Extended visible light harvesting and boosted charge carrier dynamics in heterostructured zirconate–FeS_2 photocatalysts for efficient solar water splitting. *J. Mater. Sci. Mater. Electron.* **2018**, *29*, 18957–18970. doi:10.1007/s10854-018-01666-y.
13. Zulfiqar W, Javed F, Abbas G, Larsson JA, Alay-e-Abbas SM. Stabilizing the dopability of chalcogens in $BaZrO_3$ through TiZr co-doping and its impact on the opto-electronic and photocatalytic properties: A meta-GGA level DFT study. *Int. J. Hydrogen Energy* **2024**, *58*, 409–415. doi:10.1016/j.ijhydene.2023.10.140.

14. Akhtar S, Alay-e-Abbas SM, Batool J, Zulfiqar W, Laref A, Abbas G, et al. Investigation of structural, electronic and optical properties of (V+P)-doped $BaZrO_3$ for photocatalytic applications using density functional theory. *J. Phys. Chem. Solids* **2020**, *147*, 109662. doi:10.1016/j.jpcs.2020.109662.
15. Patra AS, Chauhan MS, Keene S, Gogoi G, Reddy KA, Ardo S, et al. Combined experimental and theoretical insights into the synergistic effect of cerium doping and oxygen vacancies in $BaZrO_{3-\delta}$ hollow nanospheres for efficient photocatalytic hydrogen production. *J. Phys. Chem. C* **2019**, *123*, 233–249. doi:10.1021/acs.jpcc.8b09895.
16. Shirmohammadzadeh L, Moafi HF, Shojaei AF. Highly efficient Ag-doped $Ba_{0.5}Sr_{0.5}ZrO_3$ nanocomposite with enhanced photocatalytic and antibacterial activity. *J. Clust. Sci.* **2022**, *33*, 1475–1488. doi:10.1007/s10876-021-02063-0.
17. Suhaib SA, Zhu AK, Sun J, Guo YM, Wang ST, Wang CC. High-temperature dielectric relaxations in (Ce, Y) codoped $BaZrO_3$ ceramics. *Mater. Res. Express.* **2019**, *6*, 075010. doi:10.1088/2053-1591/ab10c4.
18. Wang G, Lv S, Shen Y, Li W, Lin L, Li Z. Advancements in heterojunction, co-catalyst, defect and morphology engineering of semiconductor oxide photocatalysts. *J. Materiomics*. **2023**, *9*, 315–338. doi:10.1016/j.jmat.2023.01.006.
19. Suhaib SSA, Yuan W. Magnetic wood-based shape-stabilized phase change composite with enhanced photothermal conversion and excellent electromagnetic interference shielding performances. *Compos. Part A Appl. Sci. Manuf.* **2023**, *176*, 107040. doi:10.1016/j.compositesa.2023.107040.
20. Wang W, Wei Y, Cheng Q, Sun S. $SrNb_2O_6$ as a novel photocatalyst with wide temperature range activity for hydrogen production. *Int. J. Hydrogen Energy* **2023**, *48*, 23817–23826. doi:10.1016/j.ijhydene.2023.03.049.
21. Wang X, Wei Y, Cheng Q, Cai M, Chen J, Sun S. A novel $La_2Ti_2CuS_2O_8$ oxysulfide photocatalyst for hydrogen production from water under visible light. *Dalton Trans.* **2021**, *50*, 8680–8685. doi:10.1039/d1dt01213a.
22. Wei Y, Liu L, Wang X, Cheng Q, Cai M, Chen J, et al. A novel $La_2Ti_2Ag_2S_4O_5$ oxysulfide photocatalyst with high activity for hydrogen production from water under visible light. *Int. J. Hydrogen Energy* **2022**, *47*, 28671–28679. doi:10.1016/j.ijhydene.2022.06.142.
23. Xu S, Jiang J, Yang Y, Zhang C, Liu J, Luo S. Efficient visible light photocatalytic hydrogen evolution of 1T/2H-MoS_2 nanoflowers synthesized by hydrothermal method. *Int. J. Hydrogen Energy* **2020**, *45*, 868–878. doi:10.1016/j.ijhydene.2019.10.097.
24. Liu Y, Li M, Sun H, Cui W, Qian J, Wang Y, et al. Recent advances in morphology modulation of transition metal sulfides towards efficient electrocatalytic hydrogen evolution reaction. *J. Power Sources* **2022**, *535*, 231464. doi:10.1016/j.jpowsour.2022.231464.
25. Liu Y, Zhao L, Li J, Ma Y, Liu C, Tan X, et al. Enhanced photocatalytic H_2 evolution over MoS_2 quantum dot-modified CdS under visible light irradiation. *Appl. Surf. Sci.* **2022**, *592*, 153295. doi:10.1016/j.apsusc.2022.153295.
26. Guo S, Wang Y, Liu Y, Zou Z. Fabrication of 2D–2D CdS/MoS_2 heterojunctions for enhanced photocatalytic hydrogen production. *Appl. Surf. Sci.* **2021**, *541*, 148448. doi:10.1016/j.apsusc.2020.148448.
27. Zhang W, Fan Q, Cheng J, Zhou M, Liu S, Zeng X, et al. CdS/MoS_2 type II heterojunction with enhanced photocatalytic activity for hydrogen evolution under visible light irradiation. *Int. J. Hydrogen Energy* **2020**, *45*, 1913–1923. doi:10.1016/j.ijhydene.2019.11.071.
28. Suhaib SSA, Wu L, Wu X, Su Z, Sun S. *In-situ* growth of CdS nanoparticles on $BaZrO_3$ nano-cubes for photocatalytic hydrogen evolution under visible light. *Int. J. Hydrogen Energy* **2024**, *under review*.
29. Suhaib SSA, Wang J, Wu X, Su Z, Sun S. Ti_3C_2-derived TiO_2/g-C_3N_4 Z-scheme heterojunctions for efficient photocatalytic H_2 production under visible light. *Appl. Catal. B Environ.* **2024**, *under review*.
30. Li Y, Zhang D, Chen M, Yin W, Zhang L. Electronic structure engineering of MoS_2-based photocatalysts for efficient hydrogen evolution: A review. *J. Mater. Sci. Technol.* **2022**, *126*, 180–194. doi:10.1016/j.jmst.2022.04.041.
31. Wang Y, Li J, Xia Q, Zhang T, Sun J, Liang Y, et al. Rational design of MoS_2-based Z-scheme heterojunction photocatalysts for enhanced photocatalytic hydrogen evolution: Recent advances and future perspectives. *J. Energy Chem.* **2022**, *64*, 114–132. doi:10.1016/j.jechem.2021.04.009.
32. Gao L, Wu Y, Cui J, Fan Y, Liu Z. Constructing a MoS_2/CdS step-scheme heterojunction with strong interfacial contact for improved visible-light-driven photocatalytic H_2 evolution. *J. Alloys Compd.* **2021**, *869*, 159271. doi:10.1016/j.jallcom.2021.159271.
33. Wu H, Huang W, Wang C, Liu Y, Hu Z, Liu Y, et al. Single-atom Ni anchored on $ZnIn_2S_4$ for enhanced visible-light-driven hydrogen evolution. *Appl. Surf. Sci.* **2023**, *618*, 156669. doi:10.1016/j.apsusc.2023.156669.
34. Li X, Yu J, Low J, Fang Y, Xiao J, Chen X. Engineering heterogeneous semiconductors for solar water splitting. *J. Mater. Chem. A* **2015**, *3*, 2485–2534. doi:10.1039/C4TA04435J.
35. Pu Y, Yang L, Chen H, Wang Y, Tian Z, Zhang J. Single-atom Ni-decorated CuS nanosheets for highly efficient photocatalytic hydrogen evolution under visible light. *J. Colloid Interface Sci.* **2022**, *611*, 574–581. doi:10.1016/j.jcis.2021.12.059.
36. Li Z, Lu Y, Luo L, Luo Y, Gao H, Guo Y, et al. Constructing 0D/2D Ni@ZnS/g-C_3N_4 Z-scheme heterojunction for efficient visible-light-driven photocatalytic H_2 evolution. *Appl. Catal. B Environ.* **2021**, *297*, 120403. doi:10.1016/j.apcatb.2021.120403.

37. Wang L, Deng K, Liu J, Qiu Y, Zhang X, Yu Y. Nickel single-atom catalysts anchored on ZnS for efficient photocatalytic hydrogen evolution. *Chem. Eng. J.* **2023**, *452*, 139256. doi:10.1016/j.cej.2022.139256.
38. Liu T, Wang C, Zhu M, Wang C, Shi J, Zhao Y. Defect engineering in ZnS-based photocatalysts for enhanced visible-light-driven hydrogen evolution. *Int. J. Hydrogen Energy* **2022**, *47*, 12887–12896. doi:10.1016/j.ijhydene.2022.01.158.
39. Bai J, Wang S, Zhou L, Qiao M, Li Y, He H. Boosting photocatalytic hydrogen evolution by coupling ZnS with Ni single-atom catalysts. *J. Mater. Chem. A* **2023**, *11*, 10896–10905. doi:10.1039/D3TA00520E.
40. Yu Z, Jin R, Lin J, Wang X, Chen M, Wu Z. Enhanced charge separation and visible light photocatalytic hydrogen evolution over Ni-doped ZnS/CdS heterojunction. *ACS Appl. Energy Mater.* **2021**, *4*, 8972–8980. doi:10.1021/acsaem.1c01498.
41. Zhao Y, Zhang J, Chen C, Liu J, Zeng J, Li R. Strong metal-support interaction boosts photocatalytic H_2 evolution over Ni-decorated ZnS nanosheets. *Appl. Surf. Sci.* **2024**, *645*, 158960. doi:10.1016/j.apsusc.2023.158960.
42. Zhang Y, Liu H, Li T, Huang W, Yu T. Synergistic effect of Cu doping and Ni co-catalyst for enhanced photocatalytic hydrogen evolution on ZnS-based photocatalysts. *J. Colloid Interface Sci.* **2024**, *637*, 831–840. doi:10.1016/j.jcis.2023.10.070.